Common-Mode Current Prediction and Analysis in Motor Drive Systems for the New Frequency Range of 2–150 kHz

Ganjavi, Amir; Rathnayake, Hansika; Zare, Firuz; Kumar, Dinesh; Yaghoobi, Jalil; Davari, Pooya; Abbosh, Amin

Published in:
I E E E Journal of Emerging and Selected Topics in Power Electronics

DOI (link to publication from Publisher):
10.1109/JESTPE.2020.3006878

Publication date:
2022

Document Version
Accepted author manuscript, peer reviewed version

Common-Mode Current Prediction and Analysis in Motor Drive Systems for the New Frequency Range of 2–150 kHz

Amir Ganjavi, *Graduate Student Member, IEEE,* Hansika Rathnayake, *Member, IEEE,* Firuz Zare, *Senior Member, IEEE,* Dinesh Kumar, *Senior Member, IEEE,* Jalil Yaghoobi, *Member, IEEE,* Pooya Davari, *Senior Member, IEEE,* and Amin Abbosh, *Senior Member, IEEE*

***Abstract*—Due to the significant advances in fast switching semiconductor devices, harmonic emissions caused by the adjustable speed drives (ASDs) have been changed in terms of frequency range and magnitude. The frequency range of 2–150 kHz has been distinguished as a new interfering frequency range, disturbing the distribution networks. This paper proposes a behavioral model of an AC motor to predict the common-mode (CM) current in ASDs. An approach is presented to calculate the parameters of the model, through which the dominant impact of each element at a specific frequency is considered. Moreover, along with the proposed motor model, a system modeling strategy is presented for filter design considerations at the emerging frequency range of 2–150 kHz. To verify the effectiveness of the proposed model, real-time experiments are conducted. The results prove that the introduced model can accurately predict the resonances of the CM loop created by the motor. Consequently, the proposed model is suitable for EMI filter design covering the 2–150 kHz standard.**

***Index Terms*—Adjustable speed drive (ASD), common mode (CM), electromagnetic interference (EMI), motor model, supra-harmonics, 2–150 kHz.**

I. Introduction

ADJUSTABLE Speed Drives (ASDs) have attracted a large number of applications [1], [2] owing to the significant advances in power electronics technology. In a typical configuration of ASD, as shown in Fig. 1, the AC voltage of the grid is first converted to DC voltage via a diode rectifier followed by a DC-link filter. Then the DC voltage is converted to AC voltage through the rear-end inverter based on the Pulse Width Modulation (PWM) scheme to supply the AC motor. Increasing the switching frequency of the inverter may increase the slope rate (dv/dt) of the switch voltage to control the switching losses. As a result, a pulsating voltage with large values of dv/dt based on the PWM pattern is created between the neutral point of the motor (n) and the ground (PE), known as Common-Mode (CM) voltage (v_{CM}). This voltage excites the non-ideal stray capacitive couplings between the windings and motor frame (See Fig. 1). Consequently, an undesired CM current (i_{CM}) flows through the ground wire, injecting high-frequency (HF) harmonics back to the grid.

According to the International Electrotechnical Commission (IEC) and International Special Committee on Radio Interference (CISPR), ASD manufacturers should meet the requirements of the Electromagnetic Compatibility (EMC) for the frequency ranges of 0–2 kHz and 0.15–30 MHz [3]. Fig. 2 depicts the harmonic and conducted EMI frequency ranges classified by the EMC standard organizations.

As shown in Fig. 2, until now, there is not a clear regulation for the frequency range of 2–150 kHz though lately, there has been a great effort by the standard communities to regulate criteria for this frequency range [4], [5], [6]; subsequently, harmonics at the emerging frequency range of 2–150 kHz are known as supra-harmonics among the researchers. Indeed, the principal reason for the generated interest in the frequency range of 2–150 kHz could be attributed to the significant advances in power electronics converters, Power Line Communications (PLC) and Main Communication Systems (MCS) [7]. So far, in allegiance with the IEC Sub-Technical Committee 77A (SC77A), the 2–150 kHz frequency range is divided into 2–9 and 9–150 kHz ranges. Subsequently, due to these standardization procedures, the drive manufacturers are actively searching for designing new filters at the frequency range of 2–150 kHz.

In order to suppress the CM current flowing to the ground through the machine's parasitic couplings, EMI filters are assigned at the grid and converter sides [8]. Therefore, the model of the AC motor which precisely predicts the parasitic behavior of the machine is necessary at the design stage to plan an appropriate EMI filter. So far, many parasitic models of AC machines have been proposed for the frequency range of 150 kHz–30 MHz. However, these models are not appropriate for the filter design considerations of the emerging 2–150 kHz standard due to the fact that there was not an essential need for the filter design at this new frequency range. In order to design filters at this frequency range, designers should understand resonances to avoid assigning the switching frequency of the drive around these resonance frequencies and prevent from over designing the filters. Generally, the parasitic models of machines fall into two categories: physics-based models and behavioral models.

In regards to the physics-based models, detailed properties

A. Ganjavi, H. Rathnayake, F. Zare, J. Yaghoobi and A. Abbosh are with the School of Information Technology and Electrical Engineering, The University of Queensland, Brisbane, QLD 4072, Australia, e-mail: (a.ganjavi@uq.net.au, h.rathnayake@uq.edu.au, f.zare@uq.edu.au, j.yaghoobi@uq.edu.au and a.abbosh@uq.edu.au).

D. Kumar is with 2Global Research and Development Center, Danfoss Drives A/S, 6300 Gråsten, Denmark, e-mail: (dineshr30@ieee.org)

P. Davari is with the Department of Energy Technology, Aalborg University, Aalborg 9220, Denmark, e-mail: (pda@et.aau.dk).

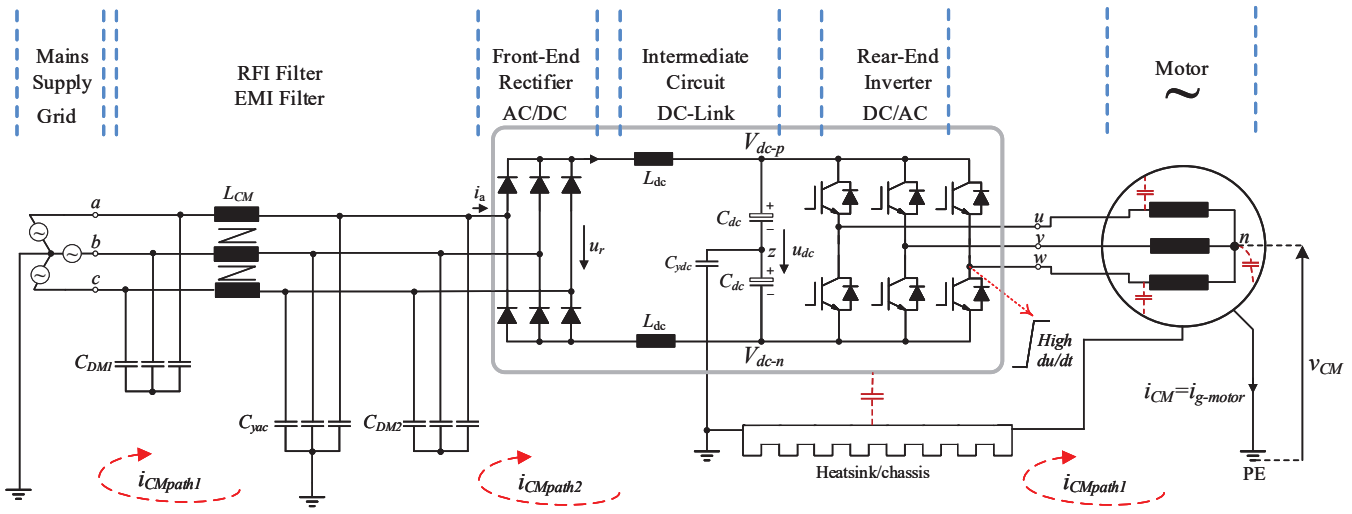

Fig. 1. Typical motor drive system.

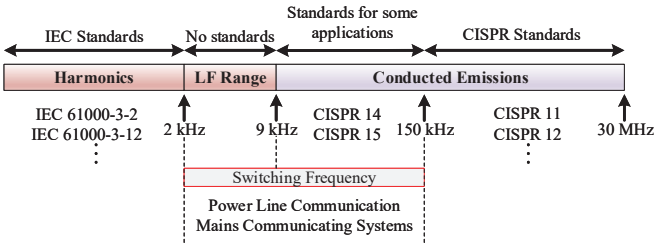

Fig. 2. Harmonic and conducted EMI frequency ranges classified by EMC standard organizations.

of the machine's material and topology are considered and the models are assigned based on numbers of equivalent circuits for each part of the machine. This can be seen in [9] and [10] where the physics-based models of the AC machines are presented. Detailed information of the machine is usually hard to access regardless if the physical information of the machine is available. The effect of this is difficulty in constructing three dimensional models of the machines, which often results in significant simulation errors [11].

In [12], [13], [14], parasitic behavior of the AC machines is predicted through behavioral models. These models are represented by a group of passive components in which the parameters are extracted through sets of experimental measurements. The main problem with these models is that often deviations between the test measurements and calculated models happen at different frequency ranges and usually high accuracy cannot be achieved through simple linear models. This could be attributed to the fact that in the real-life case, characteristics of motor dielectrics change with frequency. In practice, the features of materials namely permeability, permittivity and skin depth are dependent on frequency [15]. In [12], a behavioral model of AC motor is proposed for the frequency range of 10 kHz to 10 MHz. This model is obtained based on the vector fitting approximation in which the rational function of windings is extracted. Regardless of the challenging issues such as passivity of the equations, this method requires tedious mathematical procedures, which results in a very complicated model, consisted of multiple sub-circuits in series.

Reference [14] proposes a behavioral model of machines, in which 13 variables have been introduced for the machine model and four test measurements have been conducted to extract the variables. Moreover, in order to cope with the highly frequency dependent elements, a curve fitting method has been adopted to match the model with the measured impedances. However, the high number of measurements and curve fitting method make it very hard to extend the modeling procedure to different kinds of motors. More importantly, big differences can be seen between the measured CM impedance and the model around the resonance frequencies, degrading the usefulness of the model for the 2–150 kHz standard.

A few references have been found proposing asymmetrical topologies of behavioral models [16], [17]. These asymmetrical topologies led to simplicity of the models with good accuracy over the defined frequency range except around the resonance frequencies. Whereas the models presented in [16] and [17] are relatively simple, the skin effect and the impact of inter-winding capacitances have been neglected in order to prevent from the "trial and error" methods for adjustment of parameters. However, this will sacrifice the accuracy of the model, as differences between the calculated model and the measurements can be seen around the resonances within the range of 2–150 kHz. In fact, high accuracy around the resonance frequencies at 2–150 kHz range is of critical importance to comply with the emerging standard.

In this paper, a behavioral model of an AC machine is proposed to predict the CM current in ASDs. In order to make the model appropriate for the filter design at the emerging frequency range of 2–150 kHz standard along with the existing standards, inter-winding capacitances, skin effect and motor frame's impedance are contained in an asymmetrical topology. This combination makes the model highly accurate, which can precisely predict the detailed resonances at 2–150 kHz frequency range. Furthermore, straightforward mathematical

equations have been presented to calculate each parameters of the model. The presented calculations suggest a strategy which considers the dominant effect of each parameter at a specific frequency range rather than using the high computational algorithms or "trial and error" methods. It is worth mentioning that the high-frequency analysis for the existing 150–30 MHz standard is influenced by many other factors, such as PCB layouts, accurate switch models, enclosure model and CISPR measurement in 150 kHz to 30 MHz. On the other hand, the noise energy level at this high frequency range is much lower than the frequency range of 2–150 kHz. Consequently, with enhancing the accuracy of the model, especially at 2–150 kHz range, the proposed method can mainly be utilised as an innovative approach to design EMI filter for the emerging 2–150 kHz standard.

The main contributions of the paper can be summarized as follows:

- A new asymmetrical model of AC machine is proposed, the accuracy of which is significantly improved. This is to make the proposed model compatible with the emerging 2–150 kHz standard while the accuracy related to the existing standards is not degraded.
- A comprehensive high frequency model of a drive system with a systematic approach to model different subsystems is proposed.
- Different passive elements in a drive system for this new frequency range of 2–150 kHz have been modeled and experimentally validated.
- The proposed model of the drive system can accurately predict resonances and anti-resonances in the system, making it highly suitable for any generic or simulation based filter design at the frequency range of 2–150 kHz.

This paper is organized as follows. In section II, firstly a preliminary symmetrical model of an AC motor is presented. Section III presents the calculation and measurement methods to extract the parameters and then the issues caused by the frequency dependency problem are addressed. Moreover, in this section, in order to deal with the problems, a practical strategy is proposed to modify the model. The modified model considers the configuration of the motor windings as asymmetrical to increase the number of variables. By assigning each variable to a specific range of frequencies, the dominant parameters of the model at each frequency range can be extracted. Afterward, in section IV, real-time experiments are conducted to verify the effectiveness of the proposed model. Furthermore, a discussion is provided in section V, which gives guidance regarding the importance of the proposed model in 2–150 kHz filter design. Finally, a conclusion is provided in section VI.

II. Preliminary Symmetrical Model

In order to elaborate on the procedure that led to the proposed preliminary model of the AC motor, in Fig. 3 (a), the parasitic couplings inside an AC machine are described for one phase winding through a circuit diagram [18]. According to Fig. 3 (a), T_1 and T_2 are the winding terminals and L_w is the stator winding inductance. Moreover, C_{ws} represents the most dominant capacitor created between the windings and the stator. Also, C_w is the equivalent capacitive couplings between turns of windings as the inter-winding capacitance, which is very small compared to C_{ws}. The resistive parameters of r_s and R_w indicate the skin effect and the eddy current losses, respectively. Moreover, C_{rs} represents the capacitance between rotor and stator, and C_{wr} represents the capacitance between windings and rotor.

Apart from the aforementioned capacitive couplings, there is an impedance between the stator and frame, which can be modeled in series with C_{ws}. As the stator is grounded through the frame, this impedance should be included into the motor model. As shown in Fig. 3 (a), this is represented as R_f between the terminals and ground. In fact, R_f indicates the frequency dependency of parasitic elements due to the frame's non-ideality. This impedance has a non-linear characteristic, which could be attributed to the fact that the motor frame is made of cast iron (a group of iron-carbon alloys) while the stator is made of laminated steel. This creates grounding routes with nonlinear magnetic permeability $[\mu(f)]$.

According to Fig. 3 (a), due to the fact that C_{wr} is very small, the main CM current is generated by dv/dt through C_{ws}. In fact, the impedance consisted of the series couplings of C_{wr} and C_{rs} creates a high impedance route through which the CM current can hardly go. As a result, the rotor's effect on generating the CM current is negligible. This could be attributed to the fact that the flux penetrating into the rotor magnetic circuit at high frequency is very small [19], [20], [21]. This can be also observed in [3], [22] where the the rotor's position and speed have no important effect on mid-high frequency impedance characteristics of the machine. Therefore, to simplify the modeling procedure, the rotor of the motor can be removed. Consequently, Fig. 3 (b) shows the proposed symmetrical model of the AC motor.

III. Measurements and Calculations

Two measurement methods are adopted to extract the parasitic parameters of an AC machine. In order to calculate the parasitic parameters of the proposed model, the rotor is removed and the three phases are connected in parallel for the related tests. In this study, it is explained in detail how to extract the parameters of the proposed model in Fig. 3 (b). The first test is conducted to extract the parasitic couplings between windings and frame as C_{ws} and R_f, whereas the second test is performed to extract the parasitic couplings related to the windings as r_s, $_w$, R_w and C_w.

A. Extracting the Couplings Between Windings and Frame (C_{ws} and R_f) through Test A

The first measurement is named as Test A. In this test, according to Fig. 3 (b), a Vector Network Analyser (VNA) measures the impedance between the terminal T_1 and the grounded frame. In this section, the capacitive couplings between the windings and frame (C_{ws}) and the impedance of R_f are calculated.

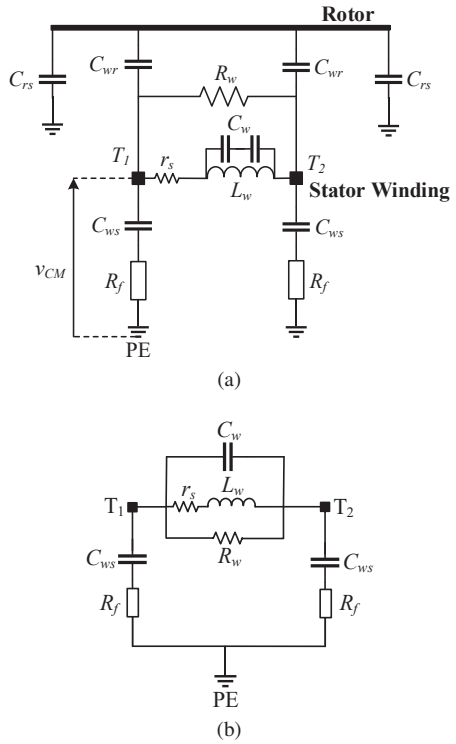

Fig. 3. AC motor structure. (a) per-phase circuit diagram with rotor [18], (b) per-phase proposed symmetrical model of the AC motor.

1) Calculation of C_{ws}: At low frequencies, which are sufficiently below the first resonance, the phase value is close to -90 degree, indicating that the equivalent impedance at this frequency range is almost capacitive. This range is described as Point 1 in Fig. 4. Generally, at low frequencies, inductive reactance (X_L) and ohmic resistance are much smaller than capacitive reactance (X_C). This can be seen in (1) and (2) when low values of frequencies (f) are substituted into the equation:

$$X_L = 2\pi f L \tag{1}$$

$$X_C = \frac{1}{2\pi f C}. \tag{2}$$

Therefore, the equivalent circuit of the proposed model at low frequencies is estimated as a pure capacitive impedance. It is worth mentioning that the value of R_f is negligible at low frequencies and it cannot be estimated at this frequency range. Accordingly, C_{ws} can be calculated using (3), in which $s = j\omega$ and Z_{AL} is the equivalent impedance of the proposed model (see Fig. 3 (b)) in Test A at low frequencies:

$$Z_{AL} = \frac{1}{6C_{ws}s}. \tag{3}$$

Consequently, by substituting the measured data at a low frequency range in (3), C_{ws} can be extracted.

2) Calculation of R_f: As previously mentioned, R_f represents the frequency dependency and the possible dielectric losses of the frame's impedance. Experiments indicate that the impedance of R_f has a resistive-inductive characteristic. However, it is understood that R_f has a dominant impact at high frequencies where the inductance value of the frame through the ground path is not significant while the resistance cannot be negligible. As a result, R_f should be calculated at high frequencies where the skin depth is very small. This frequency range is described as Point 4 in Fig. 4, which is sufficiently above the first resonance. Similar to the former analysis and due to the fact that $C_w \ll C_{ws}$, R_f can be calculated through (4), in which Z_{AH} is the equivalent impedance of the proposed model in Test A at high frequencies:

$$Z_{AH} = \frac{1}{3C_{ws}s} + \frac{R_f}{3}. \tag{4}$$

Thus, by substituting the measured data at a high frequency range in (4), the value of R_f can be extracted.

B. Extracting the Couplings Related to the Windings (r_s, L_w, R_w and C_w) through Test B

In Test B, the VNA measures the impedance between the terminals T_1 and T_2. In this section, the series winding resistance r_s, the winding inductance L_w, the parallel winding resistance R_w, and the inter-winding capacitance of C_w are extracted.

1) Calculation of r_s and L_w: The parameters r_s and L_w define the low frequency characteristic of Test B. Thus, r_s and L_w can be calculated through (5), in which Z_{BL} is the equivalent impedance of the proposed model in Test B at low frequencies:

$$Z_{BL} = \frac{r_s}{3} + \frac{L_w s}{3}. \tag{5}$$

Consequently, by equating the real and imaginary part of (5) with the real and imaginary part of the experimental measurement at a low frequency range, the series parameters of the windings can be calculated.

2) Calculation of C_w: The equivalent capacitance between turns of windings C_w defines the high frequency characteristic of Test B. At high frequency range, the resistive and inductive legs of the model (r_s, L_w and R_w) have higher impedances than the capacitive legs (C_w and C_{ws}), as seen with (1) and (2). Thus, C_w can be calculated by the following equation through the equivalent impedance of the proposed model in Test B at high frequencies (Z_{BH}):

$$Z_{BH} = \frac{2R_f C_{ws}s + 2}{6R_f C_w C_{ws}s^2 + 6C_w s + 3C_{ws}s}. \tag{6}$$

Consequently, by substituting the previously calculated values of C_{ws} and R_f in (6) and using the measurement results, C_w can be calculated.

3) Calculation of R_w: It is clear that the resistive parameters of the model are changed at different frequencies, but in order to develop a linear model, it is necessary to focus on a frequency range in which the passive elements have their dominant effects. Therefore, in order to extract R_w, the resonant frequency of the impedance has been considered since the analyzes indicate that the effect of resistance is dominant at this frequency level. Hence, R_w can be calculated through (7)–(9), where Z_B is the equivalent impedance of the proposed model in Test B at the resonance frequency:

TABLE I
CALCULATED PARAMETERS FOR THE PRELIMINARY PROPOSED MODEL OF AC MACHINE

Parameter	C_{ws}	R_f	r_s	L_w	C_w	R_w
Value	890 pF	19 Ω	9.5 Ω	11.9 pF	34 pF	15 kΩ

$$Z_B = \frac{R_w(\frac{r_s+L_w s}{3})(\frac{2R_f}{3}+\frac{2}{3C_{ws}s})}{9C_w s\alpha_1\alpha_2(\frac{2R_f}{3}+\frac{2}{3C_{ws}s}+\frac{R_w(\frac{r_s+L_w s}{3})}{9C_w s\alpha_1\alpha_2})} \tag{7}$$

$$\alpha_1 = \frac{R_w}{3}+\frac{r_s+L_w s}{9C_w s\alpha_2} \tag{8}$$

$$\alpha_2 = \frac{r_s}{3}+\frac{L_w s}{3}+\frac{1}{3C_w s}. \tag{9}$$

C. Measured and Calculated Impedances of the Static Motor

An experimental setup is prepared to conduct the test measurements. The AC machine under experiment is a 5.5 kW three-phase squirrel-cage induction motor with two poles, and the measurements are taken through the Bode 100 VNA. It is to be noted that the measurements are conducted when the motor is in static state or turned off.

Table I describes the extracted parameters of the proposed model through the calculations of (3)–(9). In Fig. 4, the comparison between the calculated model and the experimental measurements at Tests A is depicted. In fact, the impedance measured through Test A is the CM impedance of the motor, which is required for the CM loop analysis. According to Fig. 4, although there is a good match between the measurements of Test A and the model at low frequencies, deviations can be seen around the resonant and higher frequencies, which are highlighted with dashed circles in the figure. This could be attributed to the fact that in practice, parameters such as permeability, permittivity, core loss and skin effect are dependent on frequency. These issues make the calculated model deviate from the measurements at the resonant and higher frequencies. In the following sub-section, it is explained how an asymmetrical topology is proposed to deal with the frequency dependency of the parameters.

D. Modified Asymmetrical Model

1) Modification Strategy: In order to extract the capacitive couplings between the windings and stator (C_{ws}), our first try was to focus on the low frequency range (Point 1 in Fig. 4) where the phase angle of the impedance is around -90 degrees. However, according to Fig. 4, due to the frequency dependency of the dielectric materials, the capacitance of C_{ws} drops at high frequencies, resulting in large deviations between the model and test. In order to deal with this issue, two capacitors of C_{ws1} and C_{ws2}, and two resistors of R_{f1} and R_{f2} are

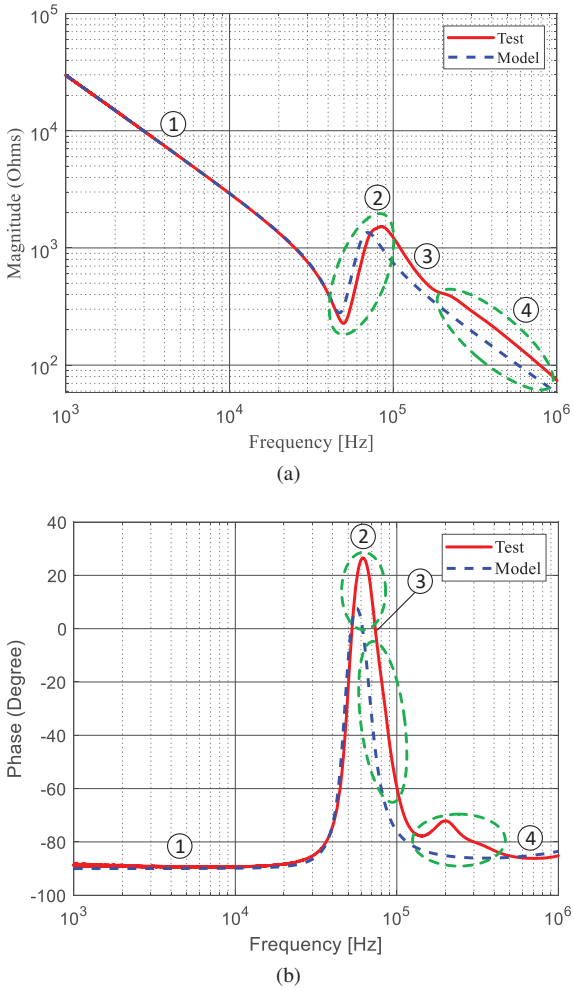

Fig. 4. Measured and calculated impedance of Test A (CM impedance) using the preliminary model. (a) Magnitude spectrum, (b) phase spectrum.

proposed in Fig. 5. Consequently, the flexibility of the model is increased through this asymmetrical model to compensate the deficiency of the model at different frequency ranges. This results in a highly accurate model that represents the detailed characteristics at 2–150 kHz.

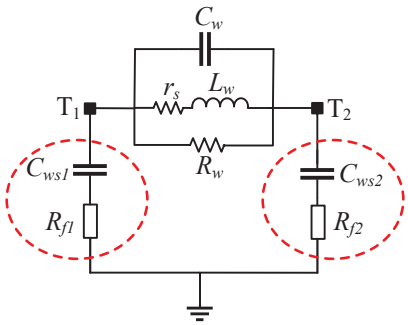

Fig. 5. Per-phase proposed asymmetrical model of the AC motor.

According to Fig. 5, to extract the parameters of C_{ws1}, C_{ws2} and R_{f1}, the equivalent circuits of the modified model at low and high frequencies should be calculated as

$$Z_{ALA} = \frac{1}{3(C_{ws1}+C_{ws2})s} \tag{10}$$

$$Z_{AHA} = \frac{1}{3C_{ws1}s} + \frac{R_{f1}}{3} \tag{11}$$

where Z_{ALA} and Z_{AHA} are the equivalent circuits of Test A based on the asymmetrical model at low and high frequencies, respectively. From (10) and (11) along with the test measurements, C_{ws1}, C_{ws2} and R_{f1} can be calculated. It is to be noted that the low frequency range is defined as the frequency sufficiently below the first resonance (Point 1 in Fig. 4) and the high frequency range is defined as the frequency sufficiently above the first resonance (Point 4 in Fig. 4).

Meanwhile, r_s is calculated using the same procedure as the symmetrical model at low frequencies. Now, in order to calculate C_w and R_{f2} for the new asymmetrical model, the high frequency equivalent circuit of Test B should be extracted. Hence, Z_{BHA}, which is the high frequency equivalent circuit of the proposed asymmetrical model at Test B, can be calculated using the following equation:

$$Z_{BHA} = \frac{\frac{R_{f1}}{3} + \frac{R_{f2}}{3} + \frac{1}{3C_{ws1}s} + \frac{1}{3C_{ws2}s}}{1 + C_w R_{f1} s + C_w R_{f2} s + \frac{C_w}{C_{ws1}} + \frac{C_w}{C_{ws2}}}. \tag{12}$$

By substituting the calculated values of C_{ws1}, C_{ws2} and R_{f1} in (12) and by equating the real and imaginary parts of the equation with the real and imaginary part of the experimental measurement at a high frequency range after the second resonance, C_w and R_{f2} can be extracted.

As seen in Fig. 4, the phase amplitude of the test measurement at the resonant frequency is higher than the calculated model. Simulation results demonstrate that with increase in the value of L_w, the model's resonant frequency is shifted to lower frequencies, indicating that L_w has its dominant impact on the resonant frequency of Test A. Moreover, the behavior of the CM impedance with variations of R_w from 25 to 85 kΩ is depicted in Fig. 6. According to Fig. 6, with increase in the value of R_w, both the magnitude and phase of the impedance at the resonance is increased though the magnitude at the anti-resonance is decreased. This indicates that R_w has its dominant impact on the magnitude of impedance around the resonance in Test A. This phenomenon is essential in designing the filters as R_w can contribute to damp the resonances of the system. In other words, the frequency dependent parameters of L_w and R_w are the dominant components around the resonant frequency. Therefore, it is recommended that L_w and R_w be calculated around the resonant frequency of Test A using (13) and (14), in which Z_{AA} is the equivalent impedance between T_1 and frame (Test A) according to the asymmetrical model proposed in Fig. 5.

$$Z_{AA} = \frac{(\frac{R_{f1}}{3} + \frac{1}{3C_{ws1}s})(\frac{R_{f2}}{3} + \frac{1}{3C_{ws2}s} + \gamma)}{\frac{R_{f1}}{3} + \frac{R_{f2}}{3} + \frac{1}{3C_{ws1}s} + \frac{1}{3C_{ws2}s} + \gamma} \tag{13}$$

$$\gamma = \frac{R_w(r_s + L_w s)}{27C_w s(\frac{R_w}{3} + \frac{r_s + L_w s}{3(1+C_w r_s s + C_w L_w s^2)(\frac{r_s}{3} + \frac{L_w s}{3} + \frac{1}{3C_w s})})}. \tag{14}$$

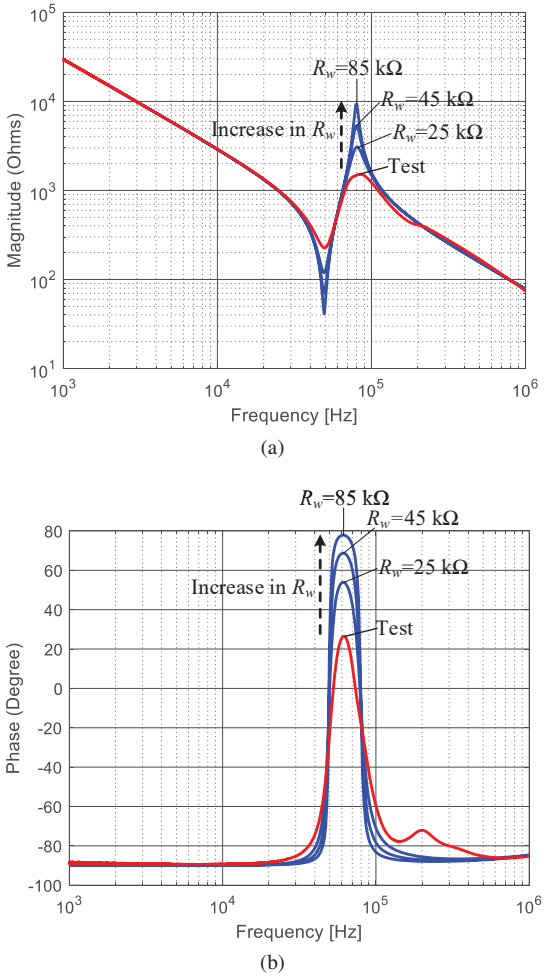

Fig. 6. Effect of R_w on CM impedance. (a) Magnitude spectrum, (b) phase Cspectrum.

Table II describes the extracted parameters for the modified asymmetrical model. Moreover, in Fig. 7, the comparison between the modified model and the test measurements is depicted. According to Fig. 7, there is an accurate match between the modified model and the test measurements of the CM impedance. By comparing the results shown in Figs. 7 and 4, it can be realized that the modified model is significantly improved, verifying the effectiveness of the asymmetrical model and recommended strategy for extracting the parameters of the AC motor.

TABLE II
CALCULATED PARAMETERS FOR THE MODIFIED ASYMMETRICAL MODEL OF THE AC MACHINE

Parameter	C_{ws1}	C_{ws2}	R_{f1}	R_{f2}	r_s	L_w	C_w	R_w
Value	680 pF	1100 pF	20 Ω	13 Ω	9.5 Ω	9.4 mH	4.6 pF	12.7 kΩ

E. Case Study Analysis for Different Types of Machines

In order to validate that the proposed asymmetrical model can be extended to different kinds of AC machines, various motors are analyzed in addition to the previously studied one.

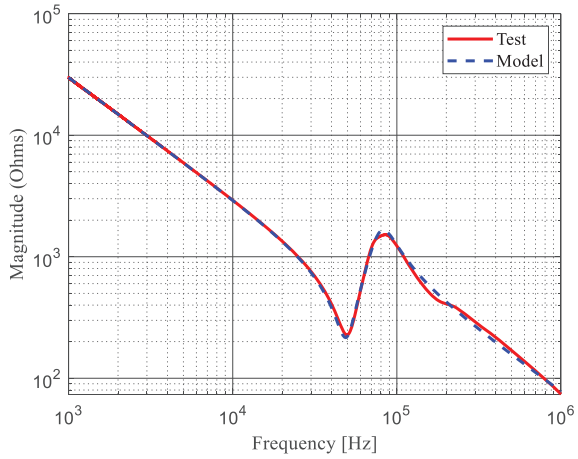

(a)

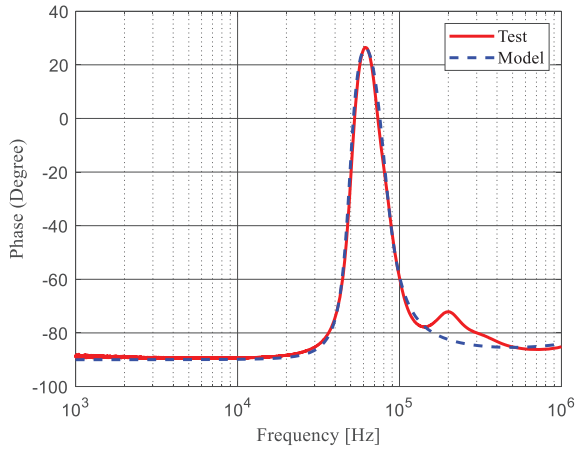

(b)

Fig. 7. Measured and calculated impedance of Test A (CM impedance) using the modified asymmetrical model (two-pole 5.5 kW squirrel-cage induction motor). (a) Magnitude spectrum, (b) phase spectrum.

Accordingly, a four-pole 1.5 kW cage induction and a 7.5 kW Permanent Magnet (PM) motor have been also analyzed through the proposed strategy. Subsequently, Table III depicts the extracted parameters of the proposed asymmetrical model for all the three kinds of machines analyzed in this paper.

In Figs. 8 (a) and (b), the comparisons between the proposed machine models and the test measurements are depicted for the 1.5 kW four-pole induction motor and the PM motor, respectively. As seen in Fig. 8, the proposed model accurately follows the measured CM impedance for different types of machines. Indeed, according to the calculated parameters depicted in Table III and the comparisons drawn in Figs. 7 and 8, it is noticed that the parasitic couplings of a machine can substantially differ depending on its type.

F. Comparative Study

Table IV describes the properties of five different HF machine models; four are of other authors and one of the authors of this paper. Among the several surveyed models, [23] and [12] have been found to suggest medium and good accuracy, respectively, in CM impedance prediction. However,

TABLE III
EXTRACTED PARAMETERS OF THE PROPOSED MODEL FOR DIFFERENT TYPES OF MACHINES

Motor type	Squirrel-cage induction	Cage induction	7.5 kW PM
Rated power	5.5 kW	1.5 kW	7.5 kW
Number of poles	2	4	6
C_{ws1}	680 pF	290 pF	250 pF
C_{ws2}	1100 pF	1370 pF	1400 pF
R_{f1}	20 Ω	1 Ω	130 Ω
R_{f2}	13 Ω	70 Ω	120 Ω
r_s	9.5 Ω	3.8 Ω	5 Ω
L_w	9.4 mH	4.93 mH	0.6 mH
C_w	4.6 pF	100 pF	150 pF
R_w	12.7 kΩ	8.5 kΩ	2.2 kΩ

the models do not cover the 2–9 kHz standard. In addition, other related issues are discussed below.

In [23], to increase the accuracy of the model, the value of parameters are extracted through the Genetic Algorithm (GA), but these optimization techniques demand large computational times, making them fairly slow [24]. Moreover, these metaheuristic methods cannot guarantee the global optimum solution of the optimization problem [25]; therefore, the most accurate model of the motor may not be achieved.

In [26], although the presented model covers a good frequency range with a good accuracy in overall, differences between the test and calculated models can be seen around the resonance frequencies. In fact, high accuracy around resonances is of critical importance to damp resonances of the system at 2–150 kHz frequency range. Moreover, in the literature, some parameters are derived based on empirical approximations. As a result, these empirical approximations cannot ensure high accuracy for different types of machines and precise calculations need to be derived.

On the other hand, in [12], to achieve good accuracy, a complex 18-order model based on sets of sub-circuits has been presented. The presented model is approximated through the Vector Fitting (VF) method, which is facing with major challenges. Firstly, the parameter conversion methods for the state-space-based HF machine model of different winding configurations are not available [26]. Secondly, the approximation methods such as VF should deal with the problems such as stability and passivity of approximations, degrading the possibility of implementation for different kinds of machines. Moreover, the presented model in [12] possesses no physic meaning for the parameters of the real-life machine; thus, the relation between the design data of the machine and the EMC requirements may not be established [16].

According to Table IV, the proposed model is more accurate around resonances, making it suitable for the emerging 2–150 kHz standards. Also, through the proposed topology and the presented strategy, the proposed model can be readily extendable to various kinds of machines.

IV. REAL-TIME VERIFICATION

In order to verify the proposed model, the CM current flowing through the Protective Earth (PE) of the motor (i_{CM})

TABLE IV
COMPARISON BETWEEN HF MACHINE MODELS

	Model [26]	Model [23]	Model [16]	Model [12]	Proposed model
Frequency range	100Hz–10MHz	10kHz–30MHz	1kHz–10MHz	10kHz–10MHz	1kHz–1MHz
Accuracy in CM impedance prediction	First resonance inaccurate	Medium accuracy	First resonance inaccurate	Accurate	Highly accurate
Equations for calculation of parameters	Partially derived	Genetic Algorithm	Partially derived	Vector Fitting	Completely derived
Number of parameters	10	13	6	18-order circuit	8
Number of measurements	2	3	2	1	2
Modeling of inter-winding capacitance	Yes	Yes	No	No physic meanings	Yes
Modeling of winding's DC resistance	No	Yes	No	No physic meanings	Yes

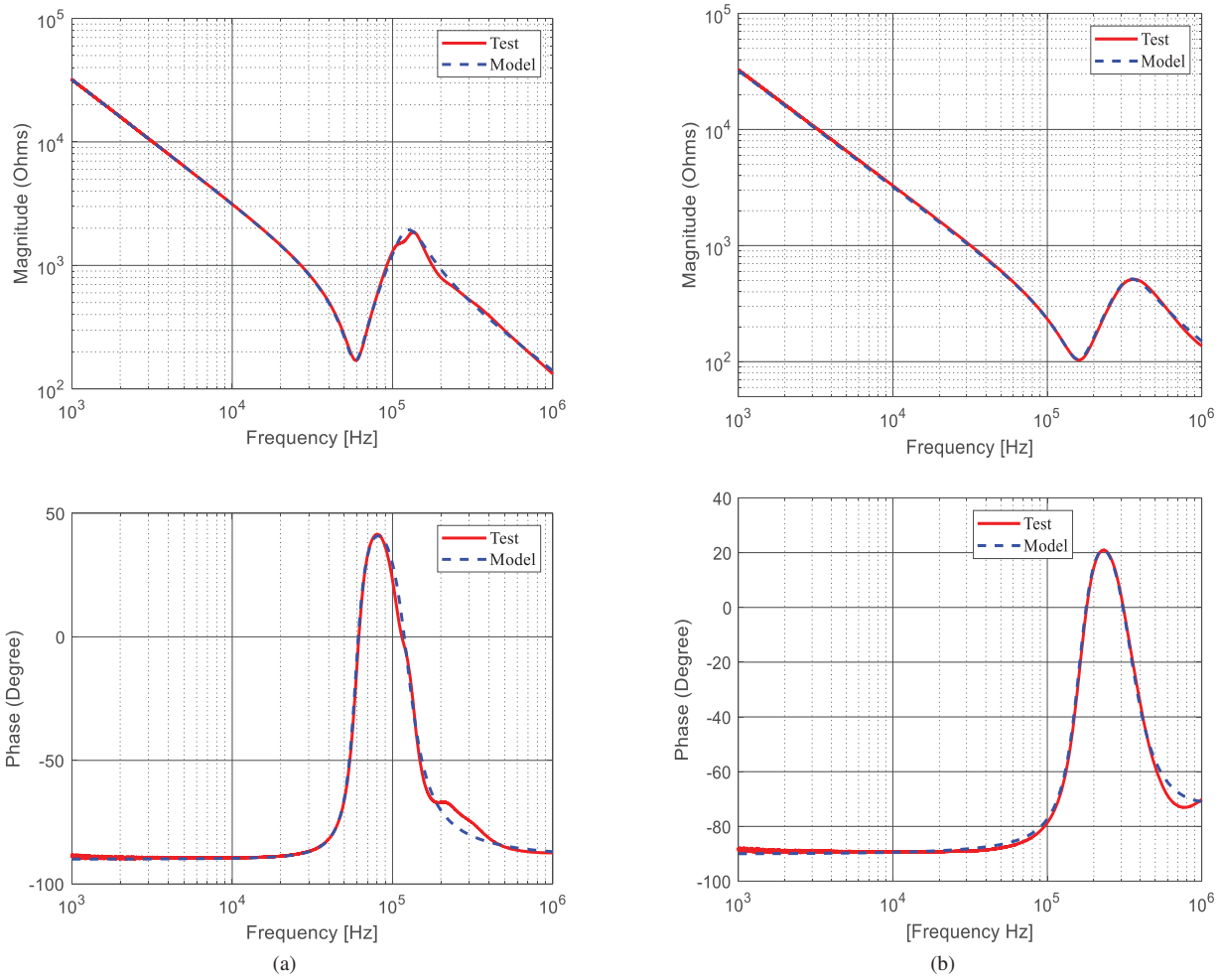

Fig. 8. Measured and calculated CM impedance using the proposed asymmetrical model for different kinds of machines. (a) four-pole 1.5 kW cage induction motor, (b) six-pole 7.5 kW PM motor.

in experiment is compared with that of the proposed modified model in simulations. Fig. 9 shows the experimental setup utilized for conducting the real-time test. In this test, the 5.5 kW AC motor at the rated speed of 3000 rpm and no-load condition is driven by a PWM inverter. The switching frequency of the inverter is 3 kHz and the switching transients are in tens of nanosecond range. Also, the maximum of dv/dt is around 2.75×10^9 volt/second. Moreover, the current probe is a Keysight N2783B with a bandwidth of 100 MHz, and the differential voltage probes are from Sapphire Instruments (SI-9110) with the bandwidth of 100 MHz. In this experiment, the pulsating voltages of the motor inputs are measured with respect to PE, using the differential voltage probes in each phase. These voltages are named to be v_{u-PE}, v_{v-PE} and v_{w-PE} (see Fig. 1). Furthermore, the current flowing through PE (i_{CM}) is measured using the high bandwidth current probe. To avoid the additional effect of cables on the results, all the measurements are conducted close to the terminal box of the motor.

Fig. 10 (a) shows the experimental results captured through oscilloscope. According to Fig. 10 (a), the voltages of the motor inputs v_{u-PE}, v_{v-PE} and v_{w-PE} pulsate with the

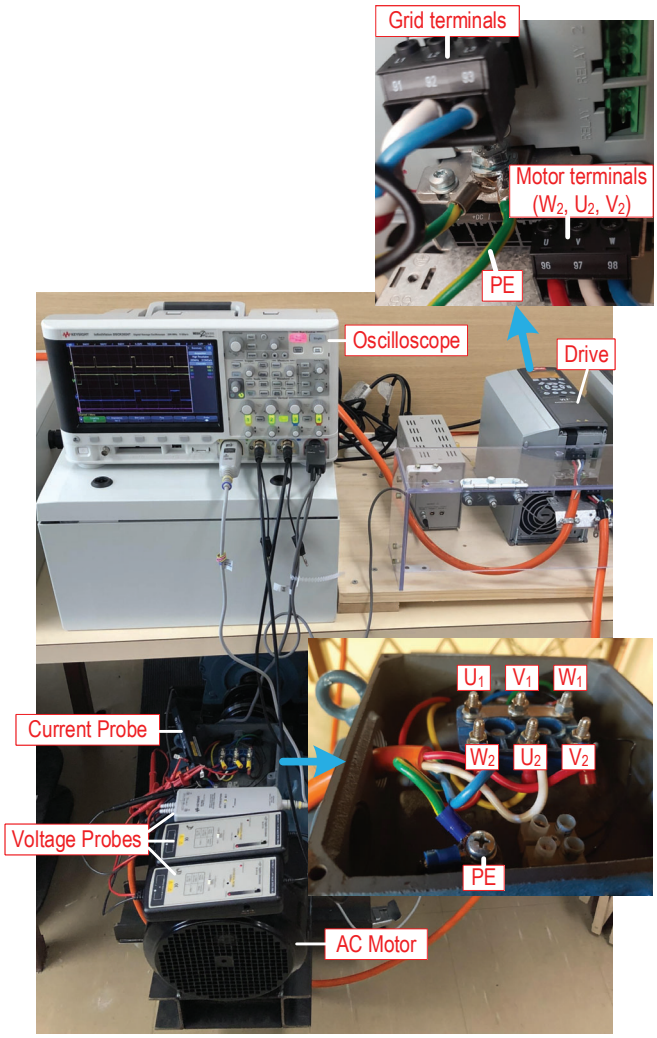

Fig. 9. Experimental setup for the real-time verification.

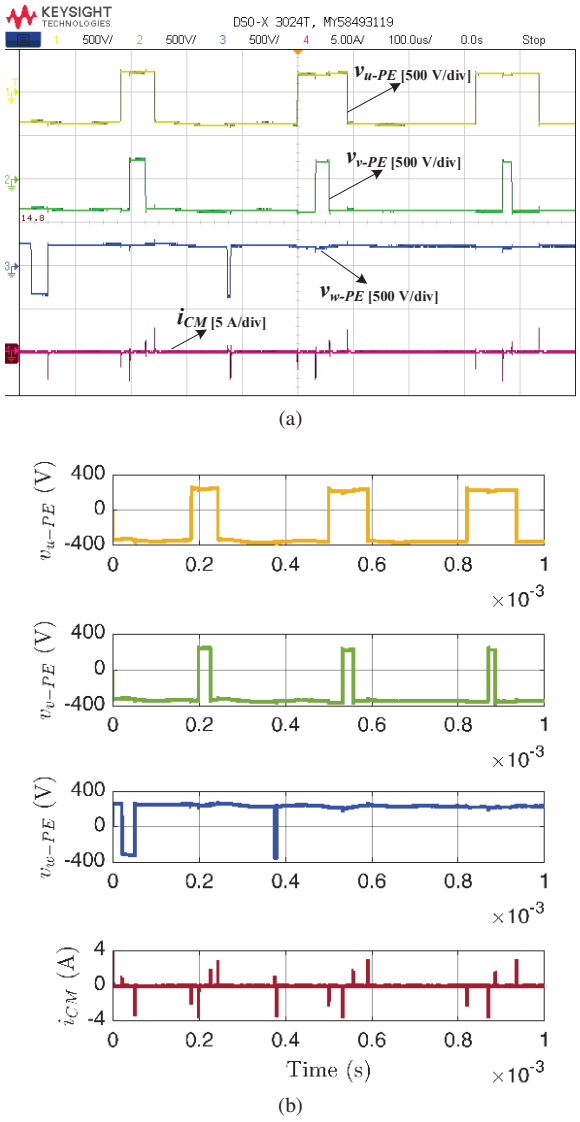

Fig. 10. CM current and pulsating voltages of the phases A, B, and C with respect to the motor input and regards to PE (i_{CM}, v_{uPE}, v_{vPE}, and v_{wPE}). (a) Experimental results, (b) simulation results.

maximum and minimum values of around 250 and -350 V, respectively. Moreover, i_{CM} has spikes with the magnitude of around 3 A. To verify the proposed model of the AC motor, the same situation should be developed in the simulation environment. To do this, the same voltage pulses of v_{u-PE}, v_{v-PE} and v_{w-PE} extracted from the experiment are assigned as the inputs of the proposed motor model in the MATLAB Simulink software. In the Simulink, the proposed asymmetrical model of Fig. 5 is used with the calculated parameters of Table II. Also, in Fig. 10 (b), the simulation results are shown.

A. Comparative Validation

In order to evaluate the competency of the proposed model, in Fig. 11, comparison between the experimental and simulation results of the CM current is depicted for the proposed model and the models presented in [16], [17]. The presented results cover the new frequency range of 2–150 kHz both in time and frequency domains. By comparing Figs. 11 (a), (b) and (c), it can be noted that the proposed model has improved the accuracy of the CM current prediction at this new frequency range. The frequency spectral contents of the CM current based on the model proposed in [16] show that accuracy of the model is highly deteriorated at 40–80 kHz range, where the accuracy of the model in [17] is affected at 20–80 kHz. Moreover, the advantage of the proposed model for the frequency range of 2–150 kHz is confirmed when comparing the time domain results in Figs. 11.

B. Accuracy of the Proposed Model at Different Powers, Rotor Speeds and Switching Frequencies

In order to analyze the accuracy of the proposed asymmetrical model at different test conditions, the line plot FFT of the experimentally measured ic_{CM} has been compared with the predicted model at different powers, rotor speeds and switching frequencies of the drive, as shown in Fig. 12. Moreover, in Fig. 12, the errors of the predictions have been plotted along with the aforementioned comparisons at each condition in the 2–150 kHz range. According to Fig. 12, the proposed model can accurately follow the experimentally

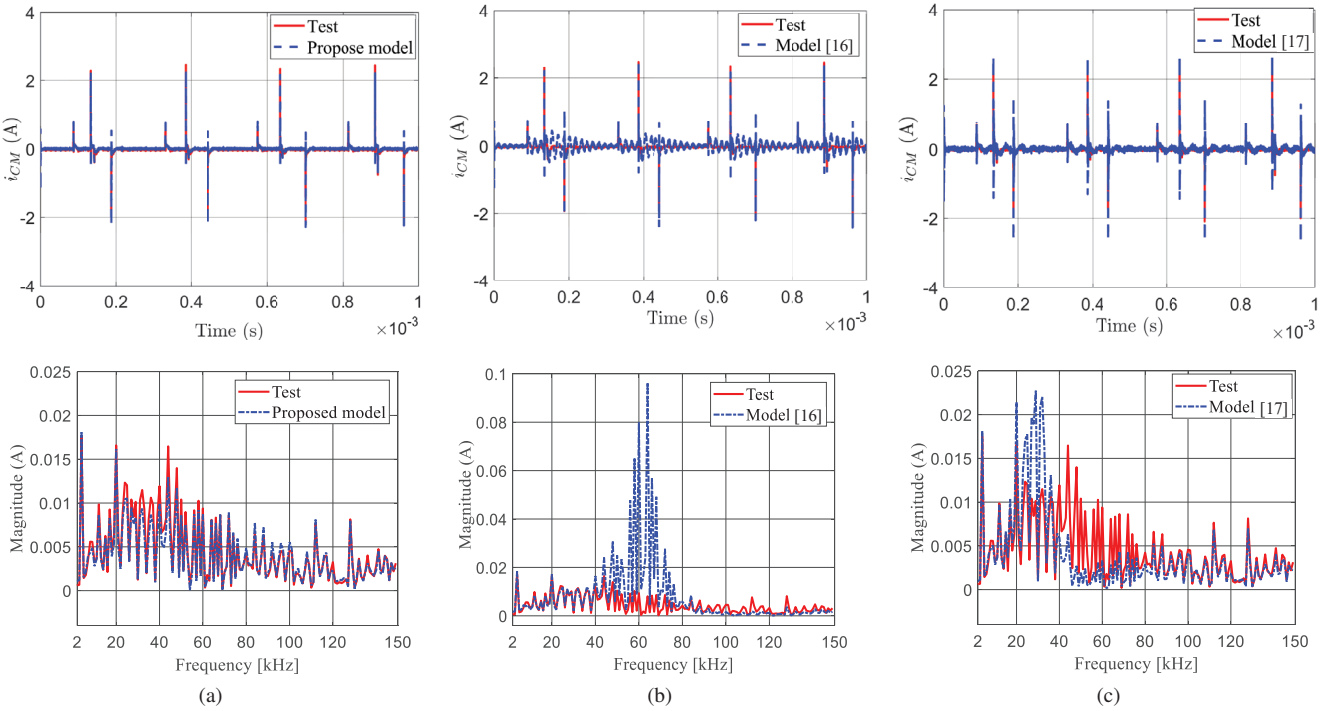

Fig. 11. Comparison between the simulated (model) and experimental CM currents of the two-pole 5.5 kW squirrel-cage induction motor in time and frequency domains, using: (a) proposed model (b) model in [16] (c) model in [17].

measured CM current at different test conditions. In order to quantitatively analyze the accuracy of the model, the Root Mean Square Error (RMSE) of the model is calculated at the different test conditions. Consequently, RMSE can be calculated as follows:

$$\text{RMSE} = \sqrt{\sum_{i=1}^{N} \frac{(\hat{y}_i - y_i)^2}{N}} \tag{15}$$

where N is the total number of frequency samples, $\hat{y}_i$ is the predicted CM current through the proposed model and y_i is the experimental CM current. Consequently, the RMSEs for different conditions of Figs. 12 (a), (b), (c) and (d) are about 0.0024, 0.0021, 0.0013 and 0.0014 A, respectively. Therefore, these very low values of RMSEs at different test conditions validate the great accuracy of the presented model.

V. Discussion on Significance of the Proposed Model for the 2–150 kHz Standard

Prediction of the complete drive system's CM current at the frequency range of 2–150 kHz is very complicated. This is due to the fact that at this frequency range, the passive components in the system are highly dependent on frequency and each one differently affects the parasitic behavior of the system. The CM choke of the EMI filter, DC choke and DC-link capacitors (see Fig. 1) are the critical frequency dependent components that need to be modeled for the parasitic analysis. In this section, accurate modeling of the above-mentioned components in the drive system is presented for up to 1 MHz.

A. Parasitic Modeling of EMI Filter

The CM transfer function of the drive's EMI filter is measured using the Bode 100 VNA. Similarly, the transfer function ($H_{CM}(f)$) of the proposed parasitic model of the EMI filter is extracted as shown in Fig. 13, in which R_{in} and R_o represent the input impedances of the VNA and LISN, respectively. According to Fig. 13, the extracted parasitic parameters of the EMI filter consists of a 5.3 mH CM choke with 29 pF parallel capacitors per phase, representing the capacitance couplings of the choke. In addition, the core losses of the CM choke is represented by 1.5 MΩ parallel resistors per phase. As seen in Fig. 14, the results related to the simulated and measured transfer functions validate the predicted model of the EMI filter for the CM analysis at 2–150 kHz.

B. Parasitic Modeling of DC Choke

DC choke also has an impact on the CM loop of the drive system. Fig. 15 shows the proposed parasitic model for the DC choke. According to Fig. 15, the DC choke consists of two DC inductors (see L_{dc} in Fig. 1) connected to each DC terminal that are packed with possible capacitive couplings, modeled as C_f. Furthermore, each inductor has an internal capacitive coupling modeled as C_{pdc} in parallel with the core losses resistor R_{pdc}. Moreover, conduction losses and skin effect of the DC choke are represented by r_{sdc}. According to Fig. 15, four terminals of the choke are named as a, b, c and d. The parameters of the proposed model are calculated through a step-by-step procedure as follows.

1) Calculation of C_f through Test 1: To calculate the parameter C_f, the impedance of Test 1 (Z_{Test1}) is measured across the terminals a and c while both a-b and c-d terminals

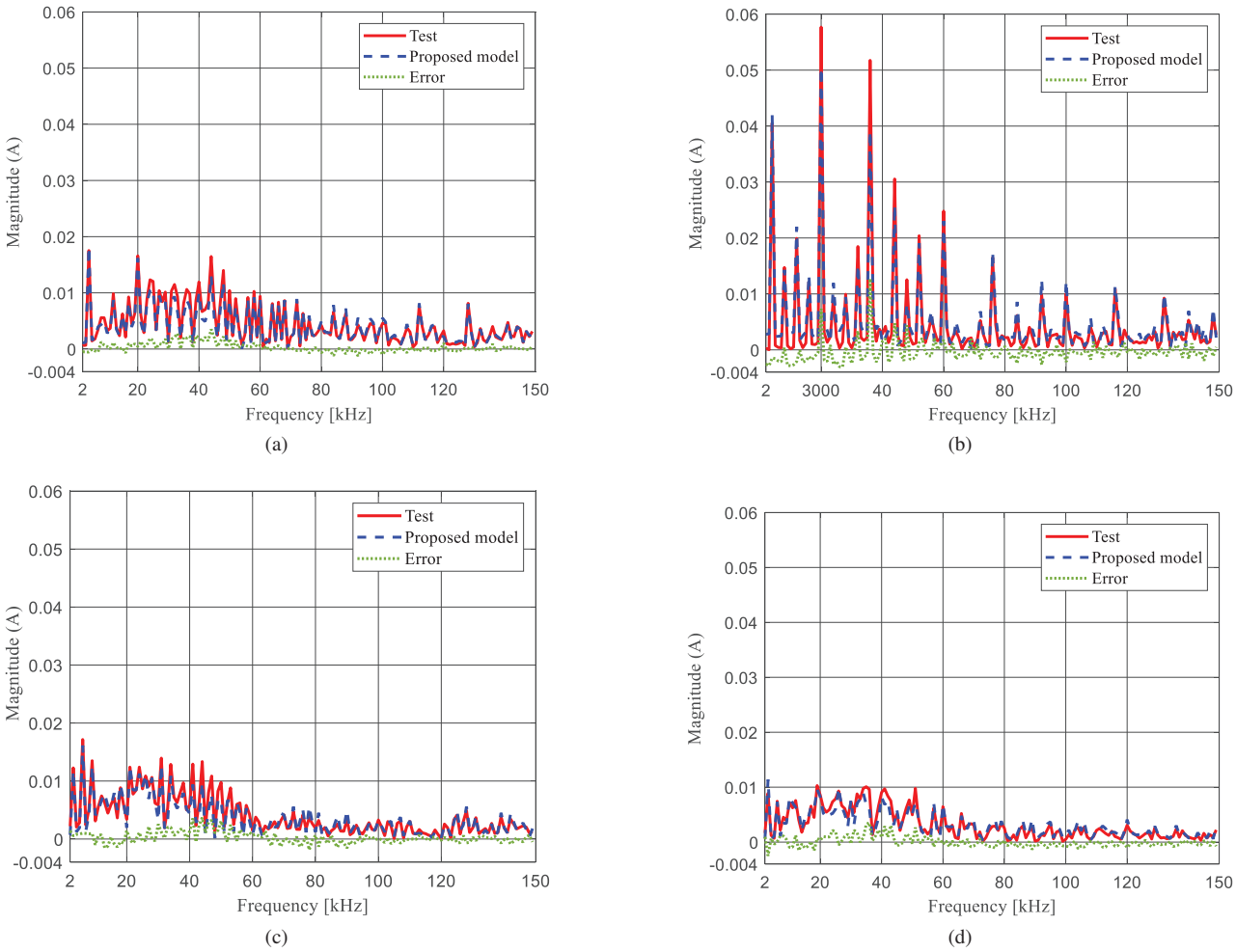

Fig. 12. Prediction of i_{CM} at different powers, rotor speeds and switching frequencies (two-pole 5.5kW squirrel-cage induction motor). (a) No-load motor with rated rotor speed (3000 rpm) at 3kHz switching frequency of the drive, (b) No-load motor with 1500 rpm rated rotor speed at 5 kHz switching frequency of the drive, (c) Half-load motor with rated rotor speed at 3kHz switching frequency of the drive, (d) Full-load motor with rated rotor speed at 3kHz switching frequency of the drive.

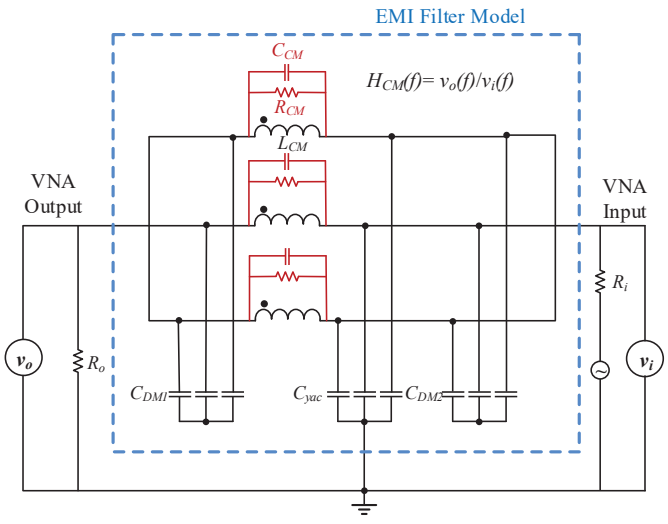

Fig. 13. Extracting the parasitic model of the EMI filter.

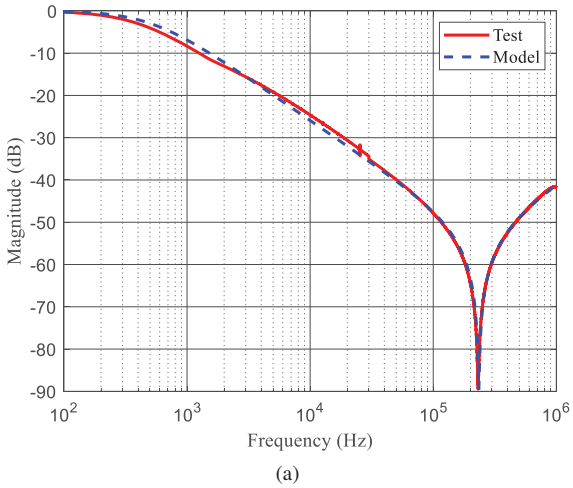

Fig. 14. Measured and simulated CM transfer function of the EMI filter using the predicted model for the CM choke.

are shorted. At high frequencies, the phase angle of the measured impedance is close to -90, so the impedance at this range is consisted of the pure capacitive couplings of C_f. Therefore, Z_{Test1} can be expressed as (16) based on the

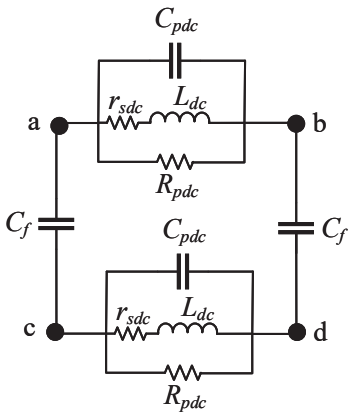

Fig. 15. Per-phase proposed parasitic model of the DC choke.

equivalent circuit of Test 1 at high frequencies:

$$Z_{Test1} = \frac{1}{2C_f s}. \tag{16}$$

Based on (16) and the measurement data, C_f can be calculated. Accordingly, Fig. 16 shows the comparison between the measurement and calculated impedance of Tets 1.

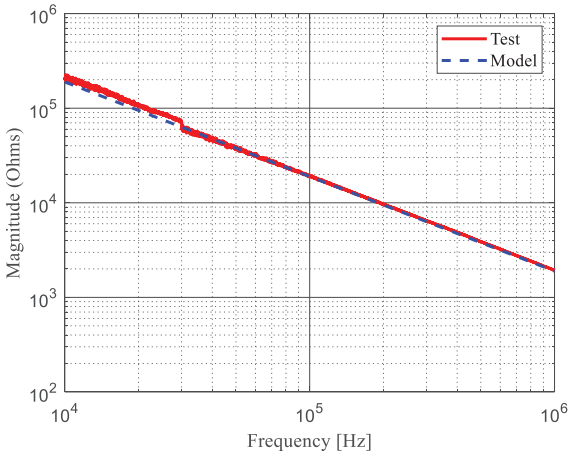

Fig. 16. Measured and calculated impedance of DC chokes through Test 1 (Z_{Test1}).

2) Calculation of L_{dc}, r_{sdc}, C_{pdc} and R_{pdc} through Test 2: To calculate the parameters L_{dc}, r_{sdc}, C_{pdc} and R_{pdc}, the impedance measurement of Test 2 is conducted between the terminals a and b while only the c-d terminals are shorted. At low frequencies, the impedance of the L_{dc}–r_{sdc} leg is very small compared to other legs, so the impedance of Test 2 at low frequencies, which is named as $Z_{Test2-L}$, can be calculated through (17):

$$Z_{Test2-L} = r_{sdc} + sL_{dc}. \tag{17}$$

Thus, by substituting the real and imaginary parts of the measured data at low frequency range in (17), the values of L_{dc} and r_{sdc} can be extracted. On the other hand, at high frequencies, the phase value of the measured impedance is around -85 degree, addressing the capacitive-resistive characteristic of the impedance. Therefore, C_{pdc} and R_{pdc} can be calculated through (18), in which $Z_{Test2-H}$ is the equivalent impedance of Test 2 at high frequency range:

$$Z_{Test2-H} = \frac{2R_{pdc}}{C_f R_{pdc} s + 2C_{pdc} R_{pdc} s + 2}. \tag{18}$$

Table V depicts the extracted parameters of the parasitic DC choke model by solving (16)–(16). Accordingly, in Fig. 17 (a), the comparison between the test measurements and the calculated impedance of Test 2 is described. According to Fig. 17 (a), there is an optimum match between the measured impedance and the calculated model at low frequency range, while a significant error can be seen from above 10 kHz. This could be attributed to the fact that in practice, characteristics of the inductive materials and core losses change with frequency due to the frequency dependency of cores' relative permeability and skin depth. In fact, the dramatic drop of magnetic permeability at high frequencies leads to saturation of the indcutors and increase in the core losses [27]. On the other hand, Fig. 17 (b) shows the comparison when the parallel resistance of the model (R_{pdc}) is reduced to 0.3225 kΩ. According to Figs. 17 (a) and (b), with decreasing R_{pdc} in value, the accuracy of the model is increased at the range of 10–100 kHz. Thus, the behavioral model of the DC chokes with constant parameters has a limitation of representing those frequency dependencies. However, it is to be noted that the DC-link filter is typically in charge of suppressing the low frequency harmonics of 0–2 kHz. Therefore, this model is considered for this paper, as our interested frequency range is 2–150 kHz. In fact, the model can cover both 0–2 kHz and 2–150 kHz ranges.

TABLE V
CALCULATED PARAMETERS FOR THE PARASITIC MODEL OF THE DC CHOKES

Parameter	C_f	r_{sdc}	L_{dc}	C_{pdc}	R_{pdc}
Value	42 pF	0.28 Ω	1.25 mH	228 pF	1.29 kΩ

C. Parasitic Modeling of DC-Link Capacitors

As seen in Fig. 1, the DC-link consists of two series connected electrolytic capacitors (C_{dc}), which create paths for the CM current towards the DC-link middle point grounded capacitor (C_{ydc}). Due to the possible frequency dependent behaviour of C_{dc} at 2–150 kHz range, a parasitic model for the DC-link capacitors is proposed as shown Fig. 18.

Moreover, in Fig. 19, the measured impedance across the capacitor using VNA is depicted. According to the test result in Fig. 19 (b), transition between the capacitive (-90 degree phase impedance) into inductive (+90 degree phase impedance) characteristic of the impedance happens. Accordingly, as shown in Fig. 18, the parasitic model of the DC-link capacitor is modeled using three parallel R–L branches in series with C_{dc}. The parameters of the suggested model can be calculated through (19), in which Z_{Cdc} is the equivalent impedance across the DC-link capacitor.

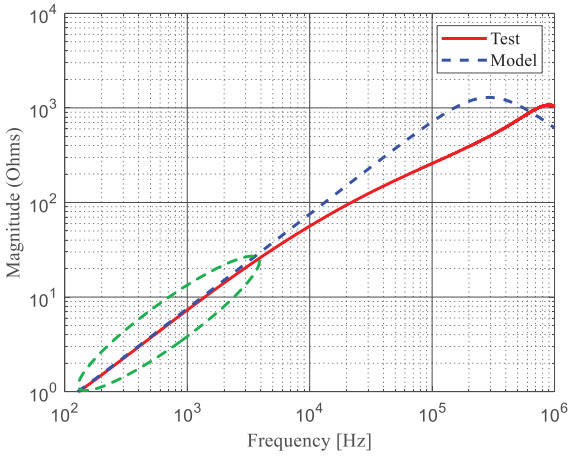

(a)

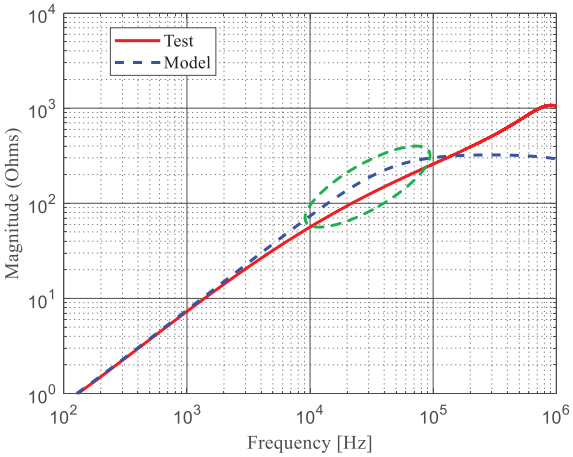

(b)

Fig. 17. Measured and calculated impedance of DC chokes through Test 2 (Z_{Test2}). (a) R_{pdc}=1.29 kΩ, (b) R_{pdc}=0.3225 kΩ.

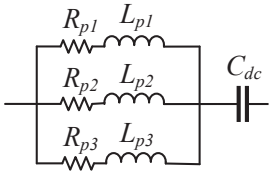

Fig. 18. Proposed parasitic model for DC-link capacitor.

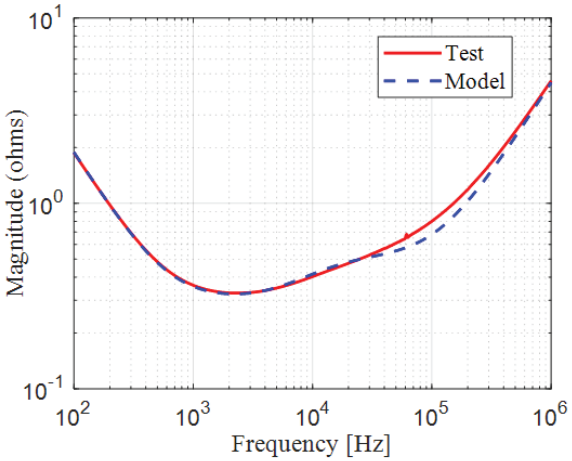

(a)

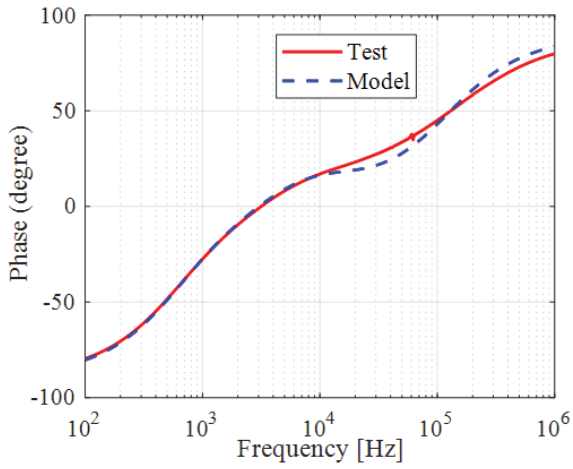

(b)

Fig. 19. Measured and modeled impedance of DC-link capacitor. (a) Magnitude spectrum, (b) phase spectrum.

TABLE VI
CALCULATED PARAMETERS FOR THE PARASITIC MODEL OF THE DC-LINK CAPACITOR

Parameter	C_{dc}	L_{p1}	L_{p2}	L_{p3}	R_{p1}	R_{p2}	R_{p3}
Value	855.5 μF	0.74 μH	30.55 μH	42.6 μH	0.54 Ω	1.13 Ω	2.26 Ω

Based on Figs. 18 and 19, the parameter C_{dc} models the impedance of the almost purely capacitive characteristic around 100 Hz. Moreover, according to Fig. 19 (a), three different slopes of impedance can be seen after 1 kHz, which is used to model the three R–L branches to represent the inductive-resistive behavior. Table VI depicts the extracted parameters of the suggested model for the DC-link capacitors. As illustrated in Fig. 19, there is a good match between the suggested DC-link impedance model and the measured impedance up to 1 MHz.

D. Guidance on Filter Design for 2–150 kHz Standard

Resonances of the system are of major importance for designing filters at the frequency range of 2–150 kHz. At the resonance frequencies, the CM impedance of the system dramatically drops, resulting in a huge CM current flowing into the system and ground. That is why the designers should appropriately predict the resonances and take measures to prevent their occurrences. In this section, it is discussed how the accuracy of the machine's parasitic model is of major importance to predict the resonances in the system.

The three-phase motor drive system is simulated in MATLAB software in accordance with the experimental lab setup of Fig. 1. The simulated drive system consists of the proposed asymmetrical motor model, the modeled EMI filter, DC chokes and DC-link capacitors. In this section, to maintain a fixed impedance at the grid side and to decouple the high frequency noises between the mains and the drive system, Line Impedance Stabilization Network (LISN) recommended

$$Z_{Cdc} = \frac{1}{C_{dc}s} + \frac{(sL_{p1}+R_{p1})(sL_{p2}+R_{p2})(sL_{p3}+R_{p3})}{(sL_{p1}+R_{p1})(sL_{p2}+R_{p2}) + s(sL_{p3}+R_{p3})(L_{p1}+L_{p2}) + R_{p1}+R_{p2}}. \quad (19)$$

by CISPR16 standards [7] is used for the EMI measurement at the range of 150 kHz–30 MHz. Moreover, until now, the CISPR16 LISN is also utilized in the industry for the 9–150 kHz frequency range analysis since this LISN is the only available option in the EMC measurement standards for the new frequency range of 2–150 kHz. As shown in Fig. 1, the CM paths are created in the system due to the grounded connections ($i_{CMpath1}$, $i_{CMpath2}$ and $i_{CMpath3}$). Also, the origin of the CM current is the AC motor, shown as $i_{CM} = i_{g-motor}$ in Fig. 1. In order to investigate the resonances within this CM loop ($i_{CMpath1}$), the same conditions in alliance with the experimental tests in Section IV have been conducted in the simulation platform, in which the inverter is driven by PWM technique at the switching frequency of 3 kHz. It is explained in the following that how the resonances of the system can be predicted through the system components modeling and how the AC machine's parasitic model has a major impact on these resonances.

In Fig. 20, the equivalent CM circuit of the three-phase drive system is extracted by paralleling the CM noise paths. In this circuit, the CM noise source in the three-phase system is the CM voltage generated by the PWM switching at the inverter terminal that can be derived in the following. Subsequently, according to Fig. 1, the CM voltage can be derived through the following procedure [28]:

$$\begin{aligned} v_{un} &= v_{uz} + v_z - v_{CM} \\ v_{vn} &= v_{vz} + v_z - v_{CM} \\ v_{wn} &= v_{wz} + v_z - v_{CM} \end{aligned} \quad (20)$$

where the CM voltage v_{CM} is defined as the voltage between the neutral point of the motor (n) and ground (PE) (see Fig. 1). Also, v_{uz}, v_{vz}, and v_{wz} are the voltages between the DC-link midpoint (z) and the motor input terminals of u, v and w, respectively. Also, v_z is the voltage between z and PE. Subsequently, according to (20) and assuming that the system is balanced, v_{CM} can be extracted from as follows:

$$v_{CM} = \underbrace{\frac{v_{uz}+v_{vz}+v_{wz}}{3}}_{v_{CM-HF}} + \underbrace{v_z}_{v_{CM-LF}}. \quad (21)$$

As can be seen in (21), the CM voltage consists of the high and low frequency terms, described as v_{CM-HF} and v_{CM-LF}, respectively (see Fig. 20). It is worth mentioning that v_{CM-HF} is generated by the PWM output voltage through the inverter, while v_{CM-LF} is generated by the grid side voltage through the diode rectifier.

According to Figs. 1 and 20, there are two filtering components in the CM loops which are: 1) the EMI filter with the CM choke (L_{CM}) and the CM grounding capacitors (C_{yac} and C_{ydc}) 2) the DC-link filter including the DC choke (L_{dc}) and DC-link capacitors (C_{dc}). To estimate the CM resonances due to all these L–C components, the frequency response of the Thevenin impedance across the high-frequency CM noise source (Z_{T-HF}) is extracted as shown in Fig. 21. According to Fig. 21, it is predicted that three resonances occur in the system, which the first one is due to parasitics of the EMI filter, the second DC choke parasitics (around 20 kHz) and the third is due to the AC machine's parasitics (around 50 kHz). Moreover, according to Fig. 21, it can be seen that with the 100% error in the parameters C_{ws1} and C_{ws2} of the motor model, the model predicts that not only the resonance frequency shifts from 50 to 36 kHz but also the magnitude of the CM impedance drops. This evaluation addresses the critical importance of the machine model's accuracy as it has a great impact on resonances and CM impedance magnitude of the system at the frequency range of 2–150 kHz. In other words, the EMC compatible drives should be designed based on the worst possible cases in the system, in which the motor plays a critical role in the design at the emerging 2–150 kHz standard. Therefore, it is important that the designers understand the impact of the parasitic motor model on the CM resonances to avoid assigning the switching frequency of the drive at these resonance frequencies. As a result, in order to design the EMI filters for the 2–150 kHz standard, the designers should extract a highly accurate motor model to avoid over designing, leading to a compact and optimized EMI filter in the system.

The presented models of Figs. 20 and 21 are validated through an experimental test measurement. Subsequently, Fig. 22 depicts the comparison between the simulated and experimentally measured high-frequency Thevenin impedance (Z_{T-HF}). Accordingly, Fig. 22 (a) describes the comparison between the test measurement and the model when the core losses resistor of DC choke is assigned at R_{pdc}=1.29 kΩ in the simulations. Also, Fig. 22 (b) is the comparison when the core losses resistance value of DC choke is reduced to R_{pdc}=0.3225 kΩ in the simulations. According to Fig. 22 (b), when the damping factor of DC choke is increased, the second resonance is also disappeared, resulting in the accurate matching of the measurement and model. This is also in compliance with Fig. 17, in which the model's accuracy increased in the range of 10–30 kHz when the core losses are increased (or the value of R_{pdc} is reduced). Moreover, this is totally in compliance with the experimental FFT spectrum of i_{CM} of Fig. 11 (a), in which resonance can seen at around 50 kHz.

VI. Conclusion

This paper proposed a behavioral model of an AC motor to predict the CM current in ASDs. The proposed model is highly useful to design EMI filters at the frequency range of 2–150 kHz by taking into account the skin effect, inter-winding capacitances and non-linearity of the motor frame. Moreover, in order to maintain a detailed accurate model, the configuration of the modeled windings are considered as asymmetrical. As a result, higher accuracy is seen since additional parameters are assigned to model the capacitance drops at high frequencies. The asymmetrical model is calculated based on

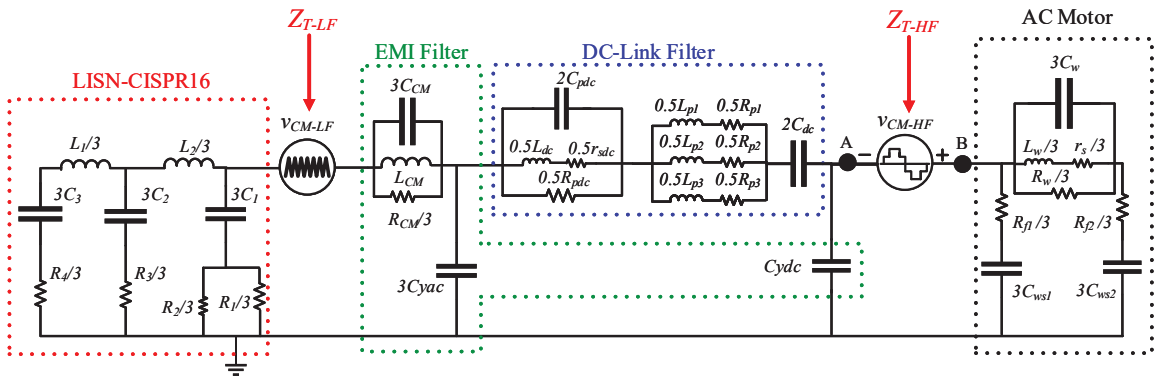

Fig. 20. Equivalent CM noise model of the three-phase motor drive system.

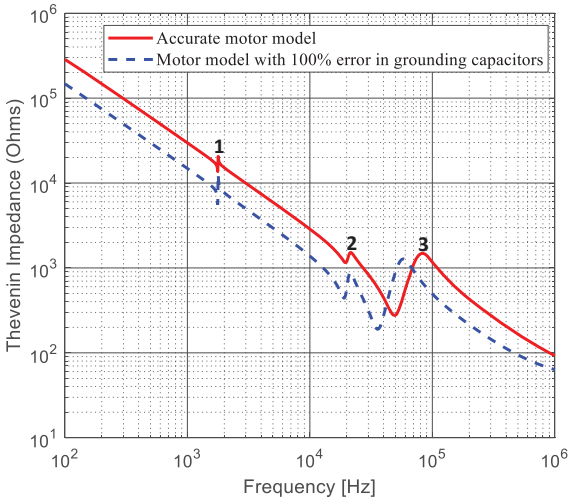

Fig. 21. Thevenin impedance across the high-frequency CM noise source model (Z_{T-HF}).

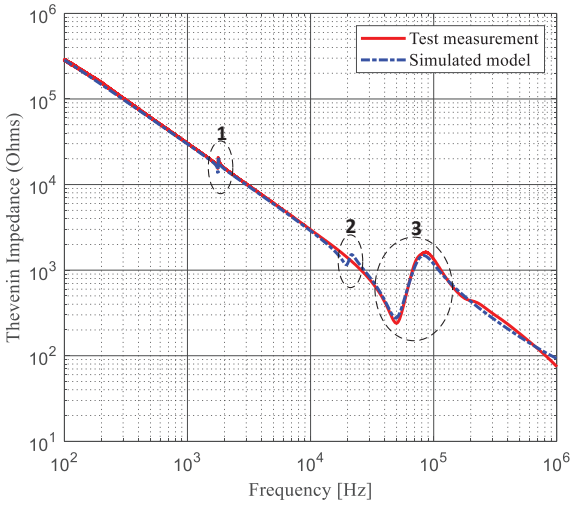

(a)

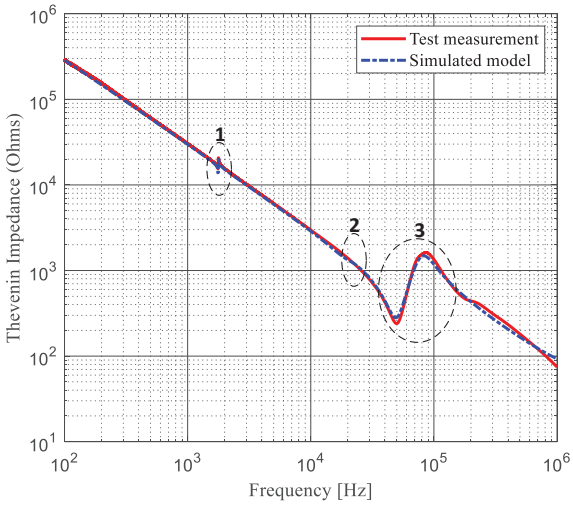

(b)

Fig. 22. Comparison between the measured and calculated Thevenin impedance of drive system (Z_{T-HF}). (a) When R_{pdc}=1.29 kΩ assigned in the model, (b) when R_{pdc}=0.3225 kΩ assigned in the model.

the dominant impact of each parameter at a specific frequency range. Along with the frequency domain measurements, the model is verified using the experimental tests of the operating motor in time domain. In addition to the proposed model of the AC motor, a system modeling strategy has been presented to provide instructions on EMI filter design for the 2–150 kHz frequency range. The results verify that the presented model can precisely predict the resonances of the CM loop created by the motor. Subsequently, the proposed motor model is highly accurate to analyze the CM current in the drive and appropriate for filter design covering the emerging 2–150 kHz standard.

REFERENCES

[1] Y. Li, H. Lin, H. Huang, C. Chen, and H. Yang, "Analysis and performance evaluation of an efficient power-fed permanent magnet adjustable speed drive," *IEEE Transactions on Industrial Electronics*, vol. 66, no. 1, pp. 784–794, Jan 2019.

[2] U. Choi, S. Jørgensen, and F. Blaabjerg, "Impact of cooling system capacity on lifetime of power module in adjustable speed drives," *IEEE Journal of Emerging and Selected Topics in Power Electronics*, vol. 7, no. 3, pp. 1768–1776, Sep. 2019.

[3] A. Boglietti, A. Cavagnino, and M. Lazzari, "Experimental high-frequency parameter identification of ac electrical motors," *IEEE Transactions on Industry Applications*, vol. 43, no. 1, pp. 23–29, Jan 2007.

[4] S. Sakar, S. Rönnberg, and M. Bollen, "Interferences in ac–dc led drivers exposed to voltage disturbances in the frequency range 2–150 khz," *IEEE Transactions on Power Electronics*, vol. 34, no. 11, pp. 11 171–11 181, Nov 2019.

[5] M. M. AlyanNezhadi, H. Hassanpour, and F. Zare, "Grid-impedance estimation in high-frequency range with a single signal injection using time–frequency distribution," *IET Science, Measurement Technology*, vol. 13, no. 7, pp. 1009–1018, 2019.

[6] K. G. Khajeh, D. Solatialkaran, F. Zare, and N. Mithulananthan, "Harmonic analysis of multi-parallel grid-connected inverters in distribution networks: Emission and immunity issues in the frequency range of 0-150 khz," *IEEE Access*, pp. 1–1, 2020.

[7] P. Davari, F. Blaabjerg, E. Hoene, and F. Zare, "Improving 9-150 khz emi performance of single-phase pfc rectifier," *CIPS 2018; 10th International Conference on Integrated Power Electronics Systems*, pp. 1–6, March 2018.

[8] X. Zhang, M. Khodabandeh, M. Amirabadi, and B. Lehman, "A simulation-based multifunctional differential mode and common mode filter design method for universal converters," *IEEE Journal of Emerging and Selected Topics in Power Electronics*, vol. 8, no. 1, pp. 658–672, March 2020.

[9] V. Mihaila, S. Duchesne, and D. Roger, "A simulation method to predict the turn-to-turn voltage spikes in a pwm fed motor winding," *IEEE Transactions on Dielectrics and Electrical Insulation*, vol. 18, no. 5, pp. 1609–1615, October 2011.

[10] N. Boucenna, F. Costa, S. Hlioui, and B. Revol, "Strategy for predictive modeling of the common-mode impedance of the stator coils in ac machines," *IEEE Transactions on Industrial Electronics*, vol. 63, no. 12, pp. 7360–7371, Dec 2016.

[11] Kohji Maki, Hiroki Funato, and Liang Shao, "Motor modeling for emc simulation by 3-d electromagnetic field analysis," in *2009 IEEE International Electric Machines and Drives Conference*, 2009, pp. 103–108.

[12] K. Jia, G. Bohlin, M. Enohnyaket, and R. Thottappillil, "Modelling an ac motor with high accuracy in a wide frequency range," *IET Electric Power Applications*, vol. 7, no. 2, pp. 116–122, 2013.

[13] G. Vidmar and D. Miljavec, "A universal high-frequency three-phase electric-motor model suitable for the delta- and star-winding connections," *IEEE Transactions on Power Electronics*, vol. 30, no. 8, pp. 4365–4376, Aug 2015.

[14] M. L. Heldwein, "Emc filtering of three-phase pwm converters," Ph.D. dissertation, ETH Zurich, 2008, pp. 82–99.

[15] Q. Deng, J. Liu, D. Czarkowski, M. K. Kazimierczuk, M. Bojarski, H. Zhou, and W. Hu, "Frequency-dependent resistance of litz-wire square solenoid coils and quality factor optimization for wireless power transfer," *IEEE Transactions on Industrial Electronics*, vol. 63, no. 5, pp. 2825–2837, 2016.

[16] O. Magdun and A. Binder, "High-frequency induction machine modeling for common mode current and bearing voltage calculation," *IEEE Transactions on Industry Applications*, vol. 50, no. 3, pp. 1780–1790, May 2014.

[17] M. Schinkel, S. Weber, S. Guttowski, W. John, and H. Reichl, "Efficient hf modeling and model parameterization of induction machines for time and frequency domain simulations," *Twenty-First Annual IEEE Applied Power Electronics Conference and Exposition, 2006. APEC '06.*, pp. 6 pp.–, March 2006.

[18] F. Zare, "Practical approach to model electric motors for electromagnetic interference and shaft voltage analysis," *IET Electric Power Applications*, vol. 4, no. 9, pp. 727–738, 2010.

[19] B. Mirafzal, G. L. Skibinski, and R. M. Tallam, "Determination of parameters in the universal induction motor model," *IEEE Transactions on Industry Applications*, vol. 45, no. 1, pp. 142–151, 2009.

[20] G. Suresh, H. A. Toliyat, D. A. Rendusara, and P. N. Enjeti, "Predicting the transient effects of pwm voltage waveform on the stator windings of random wound induction motors," *IEEE Transactions on Power Electronics*, vol. 14, no. 1, pp. 23–30, 1999.

[21] L. Wang, C. Ngai-Man Ho, F. Canales, and J. Jatskevich, "High-frequency modeling of the long-cable-fed induction motor drive system using tlm approach for predicting overvoltage transients," *IEEE Transactions on Power Electronics*, vol. 25, no. 10, pp. 2653–2664, 2010.

[22] B. Mirafzal, G. L. Skibinski, R. M. Tallam, D. W. Schlegel, and R. A. Lukaszewski, "Universal induction motor model with low-to-high frequency-response characteristics," *IEEE Transactions on Industry Applications*, vol. 43, no. 5, pp. 1233–1246, 2007.

[23] M. Degano, P. Zanchetta, L. Empringham, E. Lavopa, and J. Clare, "Hf induction motor modeling using automated experimental impedance measurement matching," *IEEE Transactions on Industrial Electronics*, vol. 59, no. 10, pp. 3789–3796, Oct 2012.

[24] B. Abdelhadi, A. Benoudjit, and N. Nait-Said, "Application of genetic algorithm with a novel adaptive scheme for the identification of induction machine parameters," *IEEE Transactions on Energy Conversion*, vol. 20, no. 2, pp. 284–291, 2005.

[25] C. Blum and A. Roli, "Metaheuristics in combinatorial optimization: Overview and conceptual comparison," *ACM Comput. Surv.*, vol. 35, no. 3, p. 268–308, Sep. 2003. [Online]. Available: https://doi.org/10.1145/937503.937505

[26] M. S. Toulabi, L. Wang, L. Bieber, S. Filizadeh, and J. Jatskevich, "A universal high-frequency induction machine model and characterization method for arbitrary stator winding connections," *IEEE Transactions on Energy Conversion*, vol. 34, no. 3, pp. 1164–1177, 2019.

[27] J. Fuzerova, J. Fuzer, P. Kollar, L. Hegedus, R. Bures, and M. Faberova, "Analysis of the complex permeability versus frequency of soft magnetic composites consisting of iron and $\mathrm{fe_{73}cu_1nb_3si_{16}b_7}$," *IEEE Transactions on Magnetics*, vol. 48, no. 4, pp. 1545–1548, 2012.

[28] S. K. Hoseini, J. Adabi, and A. Sheikholeslami, "Predictive modulation schemes to reduce common-mode voltage in three-phase inverters-fed ac drive systems," *IET Power Electronics*, vol. 7, no. 4, pp. 840–849, 2014.